

Enormous Berry-Curvature-Based Anomalous Hall Effect in Topological Insulator $(\text{Bi},\text{Sb})_2\text{Te}_3$ on Ferrimagnetic Europium Iron Garnet beyond 400 K

Wei-Jhih Zou,[○] Meng-Xin Guo,[○] Jyun-Fong Wong,[○] Zih-Ping Huang,[○] Jui-Min Chia,[○] Wei-Nien Chen, Sheng-Xin Wang, Keng-Yung Lin, Lawrence Boyu Young, Yen-Hsun Glen Lin, Mohammad Yahyavi, Chien-Ting Wu, Horng-Tay Jeng, Shang-Fan Lee, Tay-Rong Chang,* Minghwei Hong,* and Jueinai Kwo*



Cite This: *ACS Nano* 2022, 16, 2369–2380



Read Online

ACCESS |

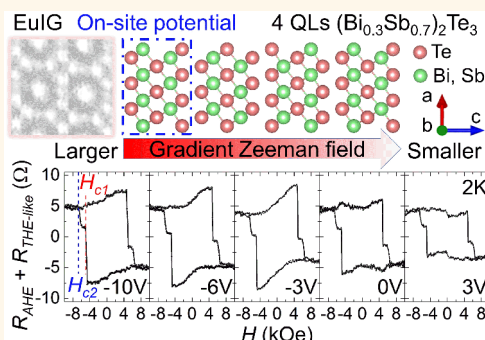
Metrics & More

Article Recommendations

Supporting Information

ABSTRACT: To realize the quantum anomalous Hall effect (QAHE) at elevated temperatures, the approach of magnetic proximity effect (MPE) was adopted to break the time-reversal symmetry in the topological insulator $(\text{Bi}_{0.3}\text{Sb}_{0.7})_2\text{Te}_3$ (BST) based heterostructures with a ferrimagnetic insulator europium iron garnet (EuIG) of perpendicular magnetic anisotropy. Here we demonstrate large anomalous Hall resistance (R_{AHE}) exceeding 8Ω (ρ_{AHE} of $3.2 \mu\Omega\cdot\text{cm}$) at 300 K and sustaining to 400 K in 35 BST/EuIG samples, surpassing the past record of 0.28Ω (ρ_{AHE} of $0.14 \mu\Omega\cdot\text{cm}$) at 300 K. The large R_{AHE} is attributed to an atomically abrupt, Fe-rich interface between BST and EuIG. Importantly, the gate dependence of the AHE loops shows no sign change with varying chemical potential. This observation is supported by our first-principles calculations via applying a gradient Zeeman field plus a contact potential on BST. Our calculations further demonstrate that the AHE in this heterostructure is attributed to the intrinsic Berry curvature. Furthermore, for gate-biased 4 nm BST on EuIG, a pronounced topological Hall effect-like (THE-like) feature coexisting with AHE is observed at the negative top-gate voltage up to 15 K. Interface tuning with theoretical calculations has realized topologically distinct phenomena in tailored magnetic TI-based heterostructures.

KEYWORDS: topological insulator, magnetic insulator, anomalous Hall effect, magnetic proximity effect, first-principles calculations, Berry curvature



INTRODUCTION

A three-dimensional topological insulator (TI) is a nontrivial state of matter hosting insulating bulk and conducting surface states (SSs) protected by time-reversal symmetry (TRS).^{1,2} The breaking of TRS at the SSs of a TI leads to the formation of an exchange gap and the emergence of chiral edge states, which gives rise to the quantum anomalous Hall effect (QAHE) with the Hall resistance quantized to h/e^2 (h is the Planck constant and e is the elementary charge.) when the Fermi level (E_F) is tuned within the exchange gap.^{3–5} Although the magnetic doping was proven to be effective in breaking the TRS, the reported QAHE observation temperature so far was less than 2 K.^{4,6–10} However, the inherent spin disorder due to the random magnetic dopants, as well as the small size of the

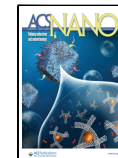
exchange gap induced by the low doping concentration, may pose an ultimate limit in raising the QAHE temperature.^{10,11}

Recently, the magnetic proximity effect (MPE) of TI/ferrimagnetic insulator (FI) heterostructures has been demonstrated to be another route of breaking the TRS.^{12–15} When a nonmagnetic TI contacts an FI with the magnetic moment perpendicular to the interface, the magnetic exchange

Received: October 1, 2021

Accepted: January 27, 2022

Published: January 31, 2022



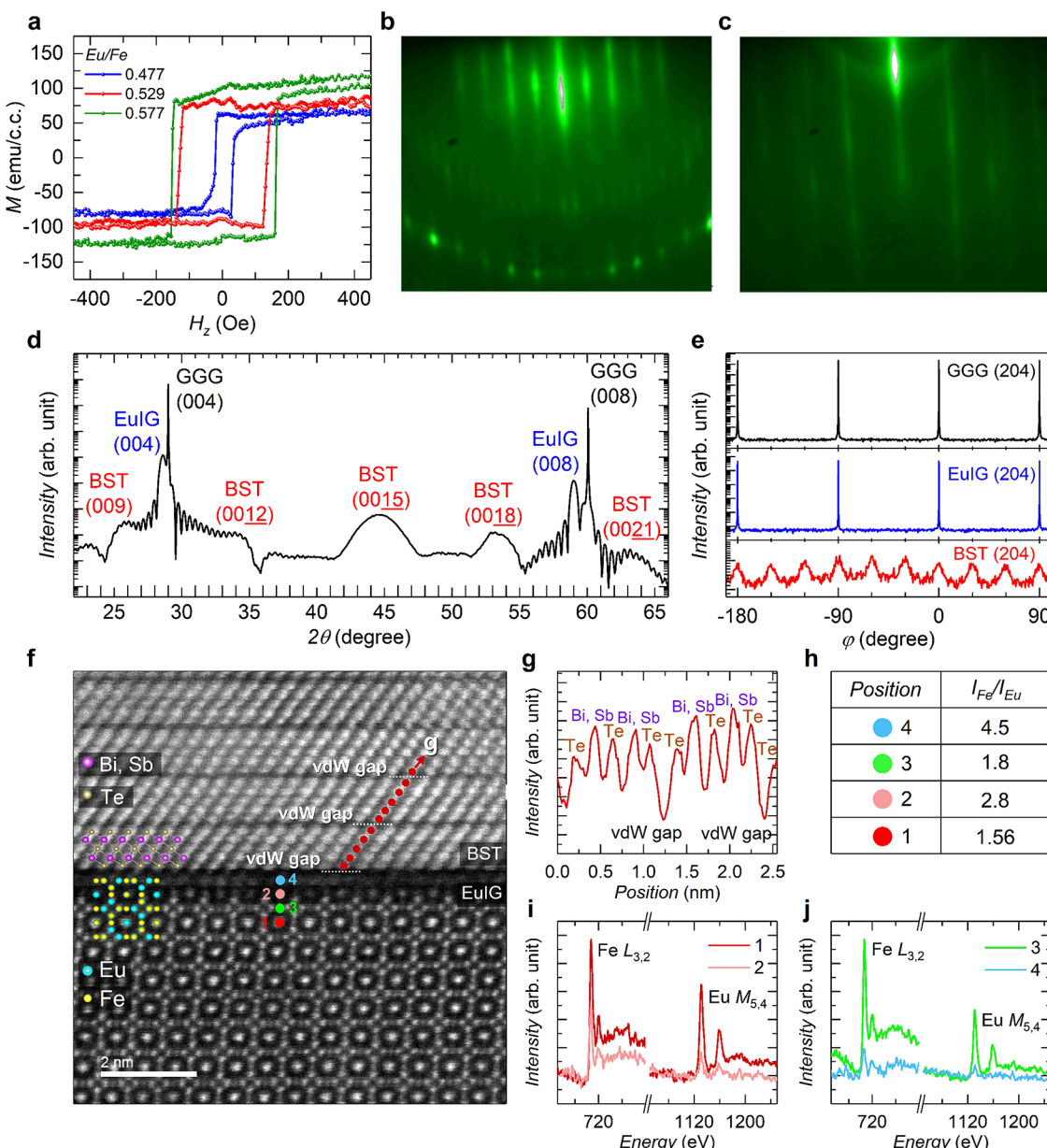


Figure 1. Magnetic and structural analysis of BST/EuIG. (a) M–H loops of EuIG films of different Eu/Fe with out-of-plane applied magnetic fields. (b and c) RHEED patterns of the EuIG(001) surface annealed at 700 °C for 30 min along the [110] axis, and the 7 nm BST(001) surface along the [100] axis, respectively. (d) XRD scan along the surface normal and (e) azimuthal φ scans crossing GGG{204}, EuIG{204}, and BST{105} reflections of BST/EuIG/GGG(001) using X-rays of 1.5498 Å wavelength. Four-domain BST was grown on single-domain EuIG with an orientation relationship of BST{100}//EuIG{100}//GGG{100}. (f) Cs-STEM HAADF image of BST/EuIG. The QLs of BST are separated by vDW gaps denoted, and the atomic arrangement in a QL (along the red arrow) is Te–Sb(Bi)–Te–Sb(Bi)–Te, which is confirmed by the intensity profile shown in g. (i and j) Position-dependent STEM-EELS spectra of EuIG near $\text{Fe } L_{3,2}$ and $\text{Eu } M_{5,4}$ edges probed at positions 1 to 4 denoted in f, and the intensity ratios are summarized in h.

interaction via the interface can open an exchange gap at the SSs of the TI. In contrast to magnetic doping, the MPE offers advantages such as fewer crystal defects causing less spin disorder, more uniformly induced interfacial magnetization, and possibly a higher ferromagnetic Curie temperature (T_c) for realizing the QAHE at significantly higher temperatures. To date, the coupling via MPE has been reported in several notable FIs [EuS, $\text{Y}_3\text{Fe}_5\text{O}_{12}$ (YIG), and $\text{Tm}_3\text{Fe}_5\text{O}_{12}$ (TmIG)]^{13,14,16,17} interfaced to TIs with the observation of an anomalous Hall effect (AHE). For example, TmIG is a high T_c (560 K) rare-earth iron garnet, and epitaxial TmIG films were grown on (111) oriented $\text{Gd}_3\text{Ga}_5\text{O}_{12}$ (GGG) by pulsed

laser deposition and magnetron sputtering.^{18–21} The magnetoelastic anisotropy due to the epitaxial strains in TmIG films on GGG-based substrates leads to the perpendicular magnetic anisotropy (PMA) of TmIG. The exchange coupling between $(\text{Bi}_{0.3}\text{Sb}_{0.7})_2\text{Te}_3$ (BST) and TmIG has resulted in a significantly enhanced T_c and the robust ferromagnetism in BST with distinctly squarish anomalous Hall hysteresis loops up to 400 K.¹⁶

Aside from TmIG, another rare-earth iron garnet $\text{Eu}_3\text{Fe}_5\text{O}_{12}$ (EuIG) with a similar T_c has gained much attention lately because of its stronger PMA field and larger coercive field (H_c) reported.^{22,23} EuIG thin films by off-axis sputtering recently

achieved by Guo et al. have shown ultrasmooth surfaces with robust and tunable PMA.²⁴ The Eu/Fe composition ratio (Eu/Fe) was finely adjusted in order to induce different degrees of compressive strain so that the magnetic properties of EuIG films were effectively manipulated, making EuIG films versatile for various spintronic applications.

In contrast to the QAHE, which originates from the Berry curvature (BC) in the momentum space, chiral spin textures due to the interfacial Dzyaloshinskii-Moriya interaction (DMI) in the real space provide the topological Hall effect (THE).²⁵ This transport signature of the nonzero spin chirality is induced by spin textures such as skyrmions stabilized by the DMI.²⁵ The DMI at the interface of TI/FI is due to the spin-orbital coupling (SOC) in TI and the broken inversion symmetry of the bilayer. Moreover, the spin-momentum locking of topological SSs makes the interfacial DMI significantly stronger than the heavy-metal-based system.²⁶ The stronger DMI strength is beneficial to form the small-sized skyrmions, thereby increasing the memory capacity per unit volume in skyrmion-based storage devices.²⁷

In this work, we report the attainment of large anomalous Hall resistance (R_{AHE}) in BST/EuIG heterostructures to high temperatures of at least 400 K. By implementing a crucial step of high-temperature annealing to the EuIG films prior to the BST growth, we succeeded in tailoring the BST/EuIG interfaces to be atomically abrupt and considerably Fe-rich. With over 35 samples fabricated, we discovered an enormous enhancement of the R_{AHE} and the ρ_{AHE} exceeding 20 times higher than the previous record at room temperature.¹⁶ Furthermore, the top-gate electrical-field effect performed on BST/EuIG showed no sign change of AHE loops with the chemical potential, consistent with our comprehensive theoretical investigation of the AHE using first-principles and the linear-response method. We identified that the AHE was indeed realized in BST because of its intrinsic Berry curvature, an artificially applied gradient Zeeman field, and an on-site potential, which simulated the MPE and the interface effect in our BST/EuIG heterostructures. Crucially, our calculations further suggest that the nearly quantized AH conductivity (AHC) within the insulating gap begins to round off as the temperature increases and makes a prominent peak of AHC. In addition, a THE-like feature was observed primarily at the negative top-gate voltage (V_{gate}) up to 15 K. The above discoveries will not only impact the study of topological phenomena, including the THE and topological magnetoelectric effect (TME), etc., but also have substantial implications for developing dissipation-less spintronic devices in the future.

RESULTS AND DISCUSSION

Material Growth and Characterization of EuIG Films and BST/EuIG Heterostructures. Epitaxial EuIG films with PMA were obtained on GGG substrates because of the positive magnetostriction constant and the in-plane compressive strain of EuIG (bulk lattice constants $a_{\text{EuIG}} = 12.49 \text{ \AA}$ and $a_{\text{GGG}} = 12.38 \text{ \AA}$).^{28,29} By tuning the substrate-to-target distance in the off-axis sputtering configuration, 23 nm thick EuIG films with increasing Eu/Fe from 0.477, 0.529, to 0.577 were grown. Squarish magnetic hysteresis loops (M–H loops) under out-of-plane magnetic fields in Figure 1a revealed the robust PMA of the EuIG films. Excessive Fe^{3+} in the EuIG films could replace Eu^{3+} in the dodecahedron sites, resulting in a stronger antiferromagnetic coupling in EuIG and a reduced saturation

magnetization (M_s). A comprehensive account of the sputtering growth and structural and magnetic properties of the EuIG films is reported elsewhere.²⁴ Figure S1 in the Supporting Information shows the atomic force microscopy (AFM) images of as-deposited and annealed EuIG films with smooth surface morphology and small root-mean-square roughness (R_q) $\sim 0.12 \text{ nm}$, essential to form an abrupt BST/EuIG interface.

BST(001) thin films were grown on EuIG(001) by an approach following the Se-buffered low-temperature (SBLT) growth method,¹⁷ where Te was substituted for Se to grow Te-based TIs. In addition, a high-temperature annealing process was implemented prior to the BST growth to improve the starting EuIG surface conditions. A EuIG film annealed at 700 °C for 30 min has led to a bright and streaky reflection high-energy electron diffraction (RHEED) pattern in Figure 1b, indicating a flat and well-ordered surface. Besides, the carbon contamination on the EuIG surface due to air exposure was significantly reduced to a minor level as diagnosed by X-ray photoelectron spectroscopy (XPS) in Figure S2a in the Supporting Information. BST thin films with a typical thickness of 7 nm were obtained, evidenced by the sharp and streaky RHEED pattern in Figure 1c. Additional BST/EuIG samples were grown with various annealing temperatures (T_a) from 450 to 750 °C on EuIG. The corresponding AFM images of the samples are shown in Figure S3 in the Supporting Information, and the smallest R_q of BST/EuIG was obtained for T_a of 650 °C.

Figure 1d shows the X-ray diffraction (XRD) scan along the surface normal of BST/EuIG/GGG with all the diffraction peaks indexed, and the c lattice constants of EuIG and GGG were determined to be 12.548 and 12.382 Å, respectively. The former value is larger than a_{EuIG} , suggesting an out-of-plane tensile strain in EuIG. The reciprocal lattice map (not shown) of off-normal reflections evidenced that EuIG is fully strained on GGG, and the EuIG lattice is thus tetragonally distorted with an elongated c -axis. Pronounced Pendellösung fringes in Figure 1d manifest the sharp interface between EuIG and GGG and the long-range order of EuIG along the c -axis. Figure 1e shows the XRD azimuthal φ scans crossing GGG and EuIG off-normal {204} reflections with peaks separated by 90°, indicating the 4-fold symmetry of both lattices. Moreover, the coincidence of GGG{204} and EuIG{204} reflections in the φ scans revealed the in-plane alignment between the two lattices. On the other hand, the φ scan crossing BST{105} (with a 3-fold symmetry) shows diffraction peaks separated by 30° instead of 120°. This finding reveals that BST consists of four rotational domains and each of them has its (100) planes aligned with one of the four EuIG{100} planes.

The spherical aberration-corrected scanning transmission electron microscopy (Cs-STEM) high-angle annular dark-field (HAADF) image in Figure 1f reveals the atomic arrangement of the sharp BST/EuIG interface with a van der Waals (vdW) gap observed. The BST stemmed from the initial Te layer on the EuIG with quintuple layer (QL) lamellae also separated by vdW gaps. The atomic arrangement of Te–Sb(Bi)–Te–Sb(Bi)–Te in a QL was confirmed by the intensity profile in Figure 1g. STEM electron energy loss spectroscopy (STEM-EELS) spectra of EuIG probed at positions 1–4 denoted in Figure 1f are shown in Figure 1i,j. The intensities of $\text{Fe } L_{3,2}$ and $\text{Eu } M_{5,4}$ were significantly decreased when the probe moved from 1 to 2 (or 3 to 4), consistent with the darker area near the top of EuIG in the Cs-STEM HAADF image. Importantly, the

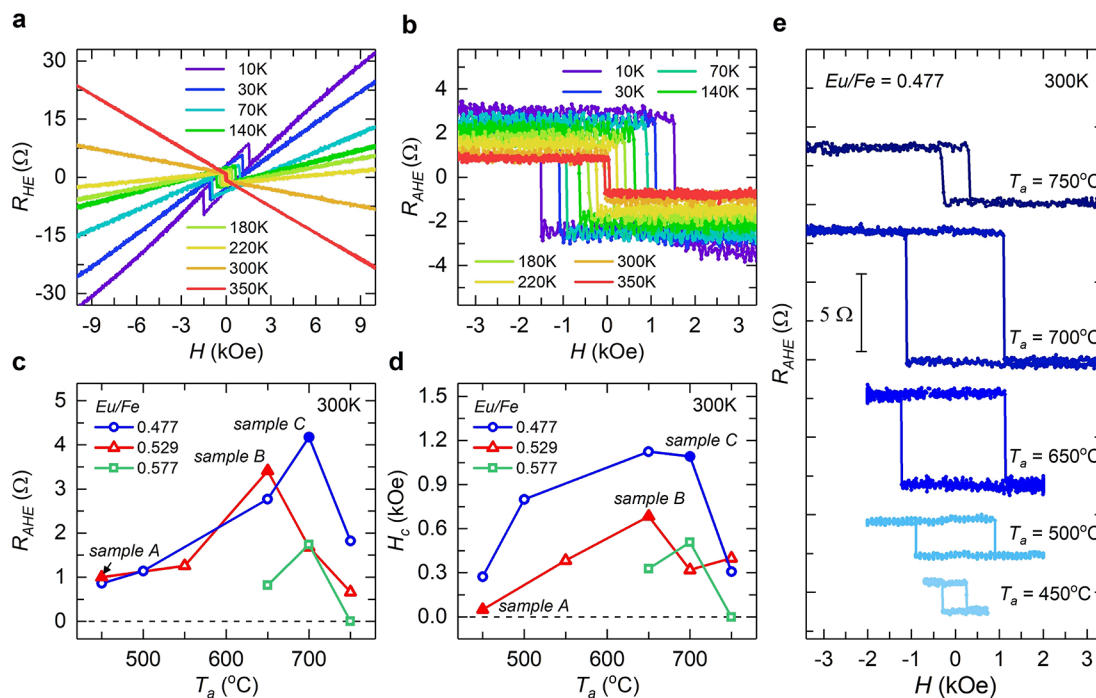


Figure 2. AHE loops varied with temperatures and growth parameters of BST/EuIG. (a) R_{HE} vs magnetic field for sample A. The Hall loops are visible in the low field region. (b) AHE loops of sample A at measurement temperatures from 10 to 350 K. (c) R_{AHE} (300 K) and (d) H_c (300 K) for samples prepared with various T_a and Eu/Fe . The solid symbols refer to samples A, B, and C. (e) AHE loops (300 K) of samples with $Eu/Fe = 0.477$ and various T_a .

intensity of Eu M_S was reduced more than that of Fe L_3 , leading to the intensity ratio of I_{Fe}/I_{Eu} increasing from 1.56 to 2.8 (or 1.8 to 4.5), summarized in Figure 1h. These results indicate lower Eu and Fe densities near the top of EuIG and that there are more Eu vacancies. Substantially the Fe-rich (over Eu) layer at the top of EuIG ~ 0.6 nm from the interface could be due to a preferential loss of EuO_x during high-temperature annealing. Higher- T_a annealed EuIG films exhibiting Fe-richer surfaces were also found by XPS, as illustrated in Figure S2b in the Supporting Information.

Tunability of Enormous AHE at Room Temperature by Varying Growth Parameters of Eu/Fe and T_a . Temperature-dependent Hall effect measurements were conducted on a series of BST/EuIG samples. In general, the EuIG and BST thicknesses were kept at 23 and 7 nm, respectively. The Hall traces of sample A ($Eu/Fe = 0.529$, $T_a = 450$ °C) from 10 to 350 K are shown in Figure 2a. As the temperature increased, the slope of the ordinary Hall effect (OHE) turned from positive to negative, in which the dominant carriers gradually changed from holes to electrons. The nonlinearity of the Hall traces was the evidence of ambipolar transport, indicating that the E_F of BST was very close to the exchange gap and far away from the bulk bands. Moreover, pronounced hysteresis loops observed in all the Hall traces illustrated the existence of AHE up to 350 K. The Hall resistances (R_{HE}) are only contributed from the BST film as EuIG is an insulating layer, and the AHE signals shown in Figure 2b were extracted by subtracting a linear OHE background between ± 10 kOe. An enormous R_{AHE} was attained ~ 0.80 Ω ($\rho_{AHE} \sim 0.56$ μΩ·cm) at 350 K. In contrast, the previous R_{AHE} record in BST/TmIG was ~ 0.18 Ω ($\rho_{AHE} \sim 0.09$ μΩ·cm) at the same temperature.¹⁶ Note that the sign of AHE in BST/EuIG remained negative despite that the conduction carriers were altered from holes to electrons with

the increasing temperature. This finding is similar to the published work on BST/TmIG¹⁶ and will be addressed further in the gate-dependent results in Figure 4. The squarish AHE loops of BST/EuIG originated from the MPE-induced ferromagnetism in BST with a gapped bottom SS due to the strong PMA of EuIG. The observation of AHE up to 350 K was benefited from the robust PMA of EuIG with a high $T_c > 400$ K.

The MPE-induced ferromagnetism in BST was realized through the exchange coupling between BST and EuIG; therefore, the interface played a critical role in leading the large AHE above room temperature. To achieve even stronger exchange coupling and AHE by tailoring the BST/EuIG interface, EuIG films were heated up to the elevated T_a prior to the BST growth. Moreover, the effect of Eu/Fe on the AHE strength was investigated at the same time. Figure 2c,d show the T_a -dependent R_{AHE} and H_c in BST/EuIG with different Eu/Fe values of 0.477, 0.529, and 0.577. Notably, large R_{AHE} values of ~ 3.41 and ~ 4.17 Ω were obtained at 300 K in sample B ($Eu/Fe = 0.529$, $T_a = 650$ °C) and sample C ($Eu/Fe = 0.477$, $T_a = 700$ °C), respectively.

The T_a -dependent R_{AHE} and H_c in Figure 2c,d exhibit a similar trend for different Eu/Fe , showing an increase for T_a from 450 to 700 °C and then a drop at 750 °C. In addition, BST grown on Fe-richer EuIG (blue dots) in general shows larger R_{AHE} and H_c , suggesting that R_{AHE} values could be correlated to the net magnetic moments of Fe^{3+} in EuIG. One published work on $Zn_{1-x}Cr_xTe/BST/Zn_{1-x}Cr_xTe$ has reported the MPE-induced QAHE by coupling between 3d-orbitals of transition metals in $Zn_{1-x}Cr_xTe$ and 5p-orbitals of Te atoms in BST.³⁰ Hence, the pronounced AHE in BST/EuIG could be attributed to the Fe-rich top layer in the annealed EuIG detected by STEM-EELS, thus favoring the coupling between 3d-orbitals of Fe and 5p-orbitals of Te.

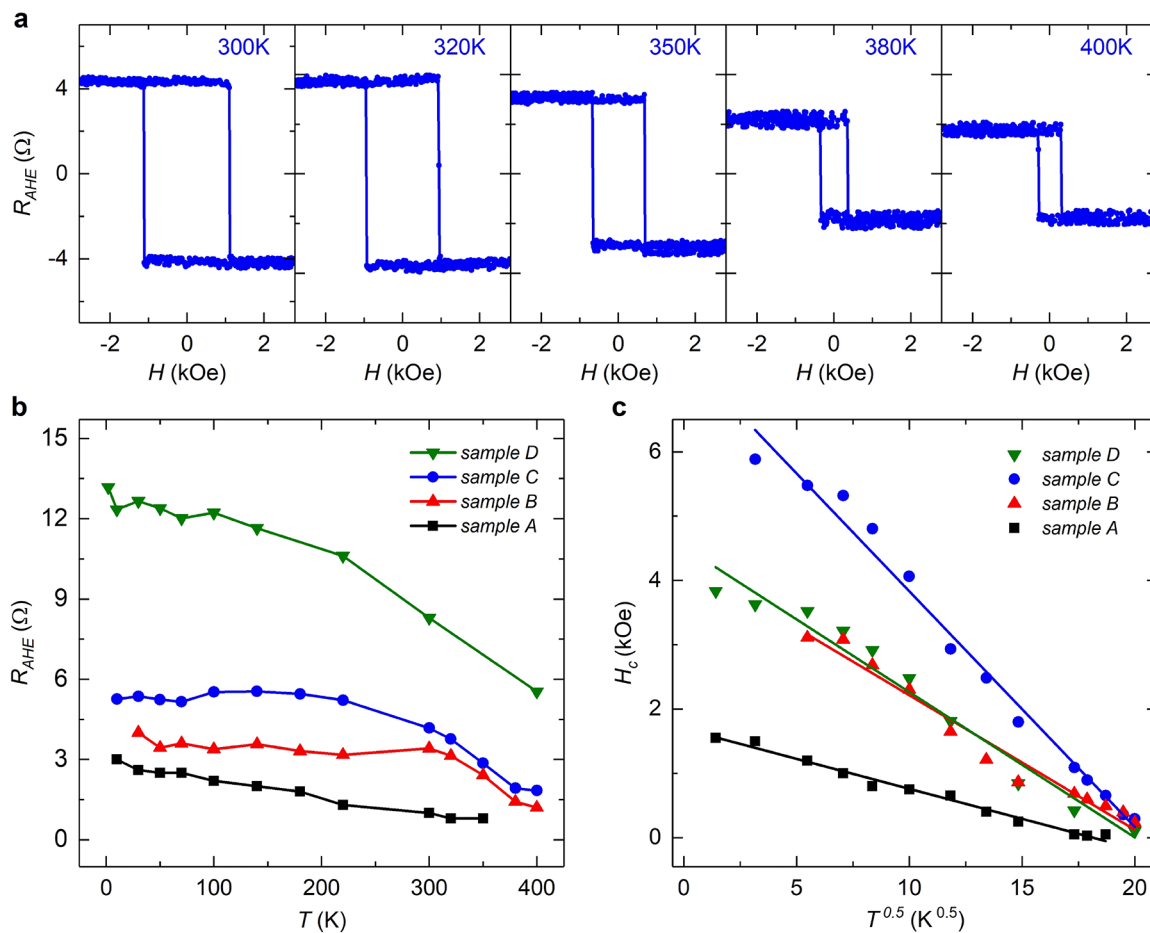


Figure 3. Temperature-dependent AHE properties of BST/EuIG. (a) AHE loops of sample C. (b) R_{AHE} of our four samples A, B, C, and D. Note that, at 300 K, ρ_{AHE} of the sample D is $\sim 3.2 \mu\Omega\text{-cm}$ higher than the previous best record $\sim 0.14 \mu\Omega\text{-cm}$ from ref 16 and exceeds the reported values from 2 to 400 K, by about about five times to forty-five times. (c) H_c of four samples in this work. The straight lines plotted in c are the linear fits of the data points.

Figure 2e displays the AHE loops of BST/EuIG measured at 300 K with $Eu/Fe = 0.477$ and increasing T_a from 450 to 750 °C, and all of them show sizable R_{AHE} . The AHE was enhanced significantly in BST/EuIG with T_a increased from 450 to 700 °C, which could be attributed to the cleaner EuIG surface with the significantly reduced carbon contamination, as well as the Fe-richer EuIG surface evidenced by the XPS data in the inset of Figure S2b in the Supporting Information. However, a sudden drop of R_{AHE} occurred for BST/EuIG with $T_a = 750$ °C, and this might be caused by the cracks of the EuIG surface shown in Figure S3f in the Supporting Information due to the overheating. Overall, the tunability of AHE strength in BST/EuIG by varying T_a and Eu/Fe of EuIG have been achieved, potential for applications in room-temperature spintronics.

Temperature Dependence of Anomalous Hall Effect. To maximize the R_{AHE} , Fe-richer EuIG with $Eu/Fe = 0.477$ was chosen to be the FI layer for stronger coupling between BST and EuIG. Figure 3a manifests the AHE loops of sample C measured from 300 to 400 K, and the R_{AHE} retained a large value of $\sim 1.84 \Omega$ at 400 K. Hall effect data above 400 K were not acquired due to instrument limitations. The large R_{AHE} values not only stand for the robustness of MPE up to 400 K but also indicate an abrupt interface between BST and EuIG with intimate contact. The squareness (SQR) of an AHE loop is defined as $SQR = \frac{R_r}{R_s}$ here, where R_r and R_s are the R_{AHE} at

the zero field and the switching field, respectively. The SQR values of all the BST/EuIG samples are approximately equal to 1.0.

The R_{AHE} values of samples A, B, C, and D from 2 to 400 K are shown in Figure 3b. The R_{AHE} values of BST/EuIG in this work surpass the previous records over 1 order of magnitude above 300 K.¹⁶ The stronger PMA in EuIG than that in TmIG could induce an enhanced spontaneous magnetization in the topological SSs of BST. The attainment of larger R_{AHE} values in BST/EuIG than those in BST/TmIG is likely caused by the outstanding interfacial quality and the stronger PMA of EuIG. The high-temperature AHE arising from the MPE in BST/EuIG and BST/TmIG implies that the T_c is above 400 K, notably superior to those of Cr- and V-doped BST reported.^{4,8,10,31} Hence, inducing a magnetic order in topological materials via MPE holds a good prospect to realize QAHE at higher temperatures than that via magnetic doping. Importantly, the BST/EuIG heterostructures with sharp interfaces can be utilized as a platform to investigate topological quantum phenomena. For example, a BST (4 nm)/EuIG (sample D, $Eu/Fe = 0.477$, $T_a = 700$ °C) was fabricated where the two surfaces are hybridized. A striking R_{AHE} value doubles to $\sim 8 \Omega$ at 300 K and monotonically increases to $\sim 13 \Omega$ at 2 K; other characteristic features that may be associated with THE emerge, as shown later in Figures 4b and 6a.^{26,32,33} In addition, the prefactor α extracted from

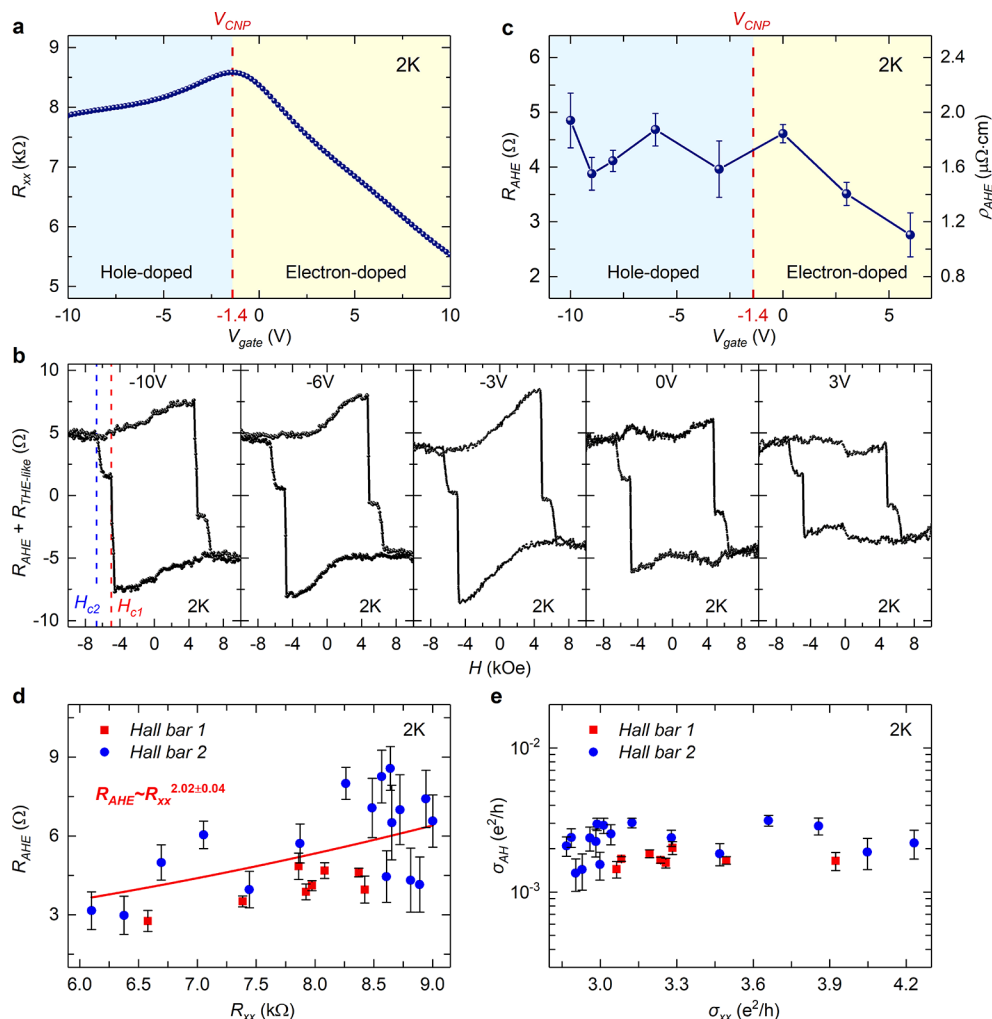


Figure 4. Gate dependence from -10 to $+10$ V at 2 K of BST/EuIG, sample E. (a) R_{xx} . (b) AHE loops. H_{c1} and H_{c2} are attributed to the coercive fields of the hybridized bottom and top surfaces of BST, respectively. (c) R_{AHE} (left) and ρ_{AHE} (right). (d) Correlation between R_{AHE} and R_{xx} showing $R_{AHE} \sim R_{xx}^{2.02}$ in two Hall bars. (e) Correlation between σ_{AH} and σ_{xx} in the same Hall bars.

the Hikami–Larkin–Nagaoka (HLN) equation is theoretically expected to be -0.5 for an independent coherence channel. We discovered an interesting trend that the α values gradually reduce to zero while the R_{AHE} values are larger, as shown in Figure S4b in the Supporting Information. The positive correlation between the R_{AHE} and the α values suggests that the strong PMA of EuIG magnetizes both the bottom and the top SSs of BST via decreasing the BST thickness in sample D.

The temperature-dependent H_c values of the AHE loops of samples A, B, C, and D are shown in Figure 3c. The robust PMA sustained at an elevated temperature with $H_c \sim 0.3$ kOe for sample C at 400 K. The H_c values in all these four samples increased significantly with decreasing temperatures. Note that the temperature-dependent H_c of M–H loops for EuIG is expected to follow the equation that describes the thermal activation of domain walls, $H_c = H_0 \left(1 - \left(\frac{T}{T_B}\right)^{0.5}\right)$, where H_0 is

the coercive field at 0 K and T_B is the blocking temperature.³⁴

In Figure 3c, the temperature-dependent H_c of the AHE follows closely with this equation, suggesting that the AHE of BST/EuIG is caused by interface effects owing to EuIG, such as MPE or the spin Hall effect (SHE). Mechanisms responsible for MPE- and SHE-induced AHE are related to exchange

coupling and SOC, respectively.³⁵ To discern the correct mechanism underlying the AHE in BST/EuIG, we investigated the dependence of the magneto-resistance (MR) on the magnetic field in out-of-plane and in-plane directions as detailed in Figure S5, Supporting Information. Markedly different trends were found between BST/EuIG and Pt/EuIG, where AHE in the latter resulted from SHE. Our analysis thus verified that AHE in BST/EuIG was induced exclusively by MPE.

Gate-Dependent Anomalous Hall Effect. To correlate the spin transport property with the electronic structure, *i.e.*, the BC near the E_F in the momentum space, the sign of the Berry-phase associated AHE component may be exploited by employing a top-gate field effect to fine-tune the chemical potential of 4 nm thick BST on EuIG (sample E) in the vicinity of the charge neutrality point (CNP). Here the electrical field extends from the top gate toward the BST layer over the entire 4 nm thickness, where the top and the bottom SSs are coupled. Detailed fabrication and measurements of the top-gate devices are described in Figure S6, Supporting Information.

Figure 4a shows the longitudinal resistance (R_{xx}) with respect to the applied V_{gate} . Maximum $R_{xx} \sim 8.5$ k\$\Omega\$ occurred at the CNP ($V_{gate} = V_{CNP} = -1.4$ V) and R_{xx} decreased in both hole-doped ($V_{gate} < V_{CNP}$) and electron-doped ($V_{gate} > V_{CNP}$)

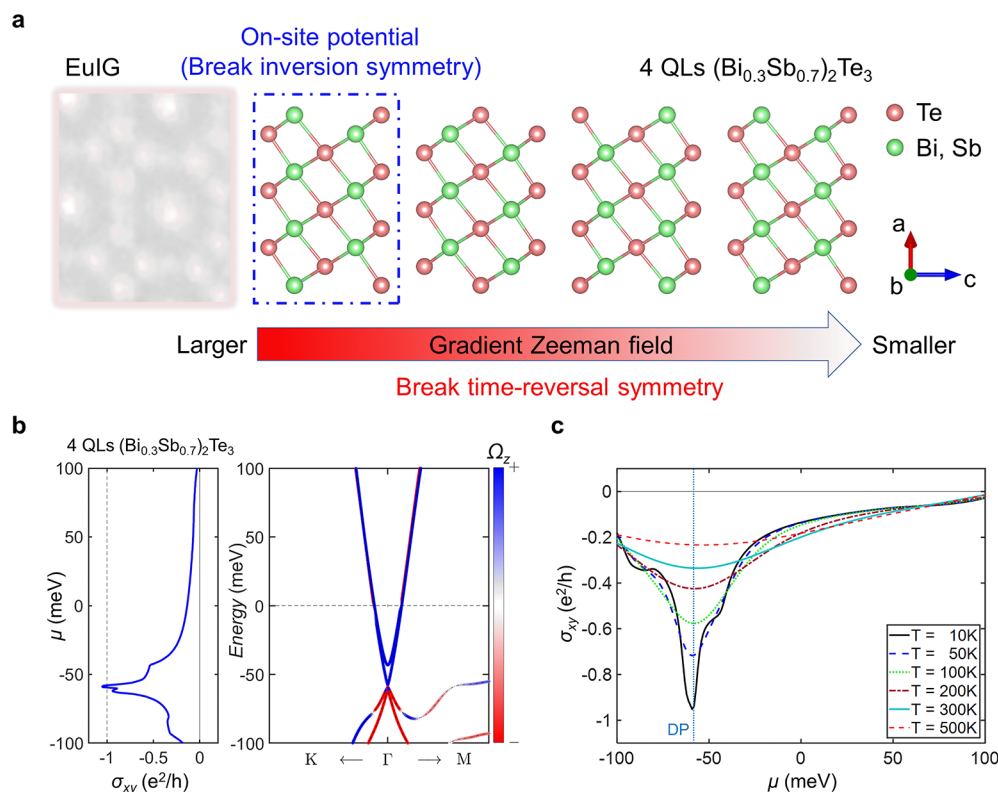


Figure 5. DFT calculations of 4 QLs BST on EuIG. (a) Model of the DFT calculations in 4 QLs BST/EuIG with a gradient Zeeman field and an on-site potential. The Zeeman field values are -40 , -30 , -20 , and -10 meV for the first QL to the fourth QL of BST, respectively; the Zeeman field here is of the exchange type. The on-site potential value is 5 meV for the 1st QL of BST. (b) Calculated local BC of each band (right) and the chemical potential dependence of σ_{xy} (left) including a gradient Zeeman field and an on-site potential at 0 K. (c) Calculated σ_{xy} of BST vs chemical potential with a gradient Zeeman field and an on-site potential as a function of temperature from 10 to 500 K.

regions. The small V_{CNP} value indicated that the E_F of the ungated BST was very close to the exchange gap.

Gate-dependent AHE loops are shown in Figure 4b, and two H_c 's (H_{c1} and H_{c2}) appear in all AHE loops. Here H_{c1} and H_{c2} are attributed to the coercive fields of the hybridized bottom and top surfaces of BST, respectively.³³ The H_{c1} and H_{c2} in all the AHE loops remained constant (~ 4.7 and ~ 6.5 kOe) over the applied V_{gate} range, independent of V_{gate} or the E_F of BST, as arising from the thermal activation of the domain walls in EuIG. Since the bottom surface of BST is in contact with EuIG, the magnetization of the bottom surface is expected to be bigger than the top surface, which causes the large jump at H_{c1} . Moreover, the surface anisotropy of the bottom surface does not manifest itself, and the induced bottom surface magnetization switches with the bulk EuIG. In contrast, the strong surface anisotropy of the top surface, due to its two-dimensional nature, thus switches at higher fields ($H_{c2} > H_{c1}$).

R_{AHE} values of sample E decrease from ~ 5 to $\sim 3 \Omega$ ($\rho_{AHE} \sim 2.0$ to $\sim 1.2 \mu\Omega\cdot\text{cm}$) when the E_F crosses from the hole-doped region to the electron-doped region as shown in Figure 4c. The R_{AHE} and R_{xx} exhibit similar behaviors that both decrease monotonically into the electron-doped region. The correlation between the R_{AHE} and R_{xx} was plotted in Figure 4d, showing a power-law dependence with an exponent of ~ 2 . To put it another way, the anomalous Hall conductivity (σ_{AH}) was nearly independent of the longitudinal conductivity (σ_{xx}), as shown in Figure 4e. The σ_{AH} can be theoretically separated into two probable contributions with different transport lifetime (τ) or σ_{xx} dependence. One is proportional to τ , which can only be attributed to the skew-scattering

mechanism; the other is proportional to τ^0 , which is attributed to the nonzero Berry phase or the side jump mechanism.^{36,37} Therefore, the relation of $R_{AHE} \sim R_{xx}^{-2}$ or $\sigma_{AH} \sim \sigma_{xx}^0$ indicated that σ_{AH} was unrelated to τ , thus ruling out the skew-scattering mechanism in BST/EuIG. Notably, the sign of R_{AHE} remained negative even though the slope of OHE changed sign in sample E, according to the gate-dependent Hall data shown in Figure S7 in the Supporting Information. This result is consistent with the temperature-dependent Hall data of sample A in Figure 2a. The unchanged sign of the AHE in BST/EuIG heterostructures results from the broken TRS and spatial inversion symmetry, which will be discussed later in the next section.

Density Functional Theory Calculations on the AHE in 4 QLs BST. To deepen our understanding the nature of unusually large AHE in BST/EuIG, we calculated the AHE of 4 QLs BST slab model based on the gauge-invariant BC in the momentum space via the density functional theory (DFT) calculations associated with the Kubo-formula approach.^{38,39} EuIG is a magnetic insulator which will provide an exchange field into the covered BST thin-film to break the TRS, and the interaction between EuIG and BST will modify the interface potential of the hybrid system to break the spatial inversion symmetry in BST. In order to match the experimental settings as much as possible, we artificially applied a gradient Zeeman and on-site energy in the 4 QLs slab model to simulate the decayed exchange field from EuIG into BST and the interface potential of the BST/EuIG interface, respectively. The calculation model with detailed parameters is illustrated in Figure 5a. Figure 5b shows the first-principles-calculated momentum- and energy-resolved BC and the corresponding

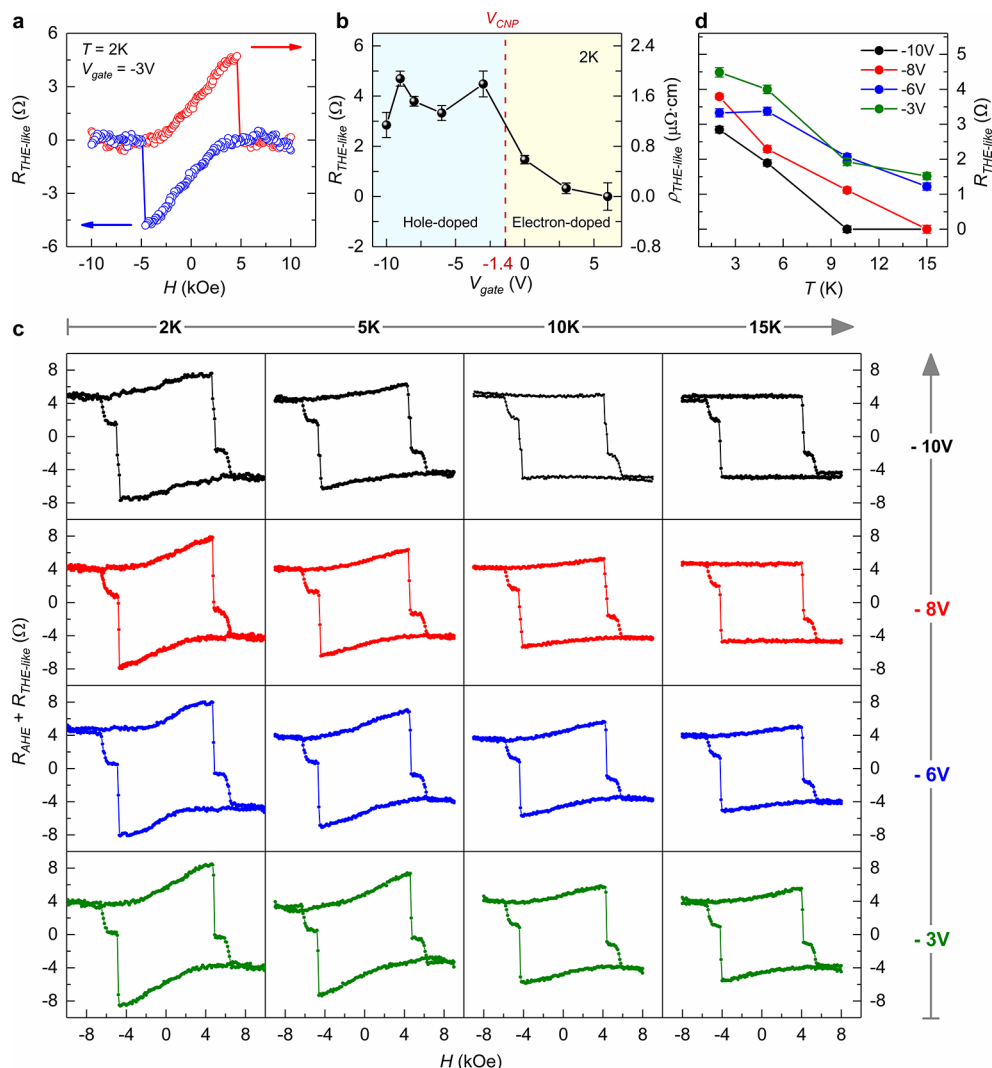


Figure 6. Observation of THE-like features in BST/EuIG. (a) Extracted $R_{\text{THE-like}}$ of sample E at -3 V and 2 K . (b) Gate dependence of $R_{\text{THE-like}}$ (left) and $\rho_{\text{THE-like}}$ (right) at 2 K . (c) Temperature dependence of AHE loops with THE-like feature. (d) $R_{\text{THE-like}}$ values for V_{gate} at -10 , -8 , -6 , and -3 V .

AHC of 4 QLs BST. The blue and red color on the band structure denotes the positive and negative value of BC, respectively. The largest AHC appears at the gapped Dirac point (DP) because of the band inverted gap. This large and nearly quantized AHC indicates that this inverted Dirac gap carries a nonzero Chern number (C), $C = 1$. It is worthy to note that the BC is not selectively strong near the DP but distributes in the wide range of the energy band. Thus, the sign of AHC remains the same and extends from -0.1 to 0.1 eV , which is consistent with our gate-dependent measurements. The AHC calculated from the Kubo formula is responsible for the intrinsic AHE, which further supports that the MPE-induced AHE in BST/EuIG is less likely caused by other disorder effects. The temperature-dependent calculations in Figure 5c reveal that the peak of AHC around the DP will be strongly suppressed with increasing temperature but persist even above room temperature, presumably caused by the topological properties of the gap near the Γ point.

As stated earlier, the full AHE can be in general attributed to three distinct contributions: Berry-curvature, skew-scattering, and side-jump contributions.³⁶ As discussed in Figure 4d, the gate-dependent results showing $R_{\text{AHE}} \sim R_{xx}^{-2}$ cannot provide

direct evidence to distinguish the Berry-curvature and side-jump contributions. It is noteworthy that the theoretical work was proposed that the side-jump induced AHE is related to Berry curvature.⁴⁰ Since there is no effective way to differentiate the Berry curvature and side-jump contributions in experiments, the working principle adopted by the community so far is to combine the Berry curvature and side-jump and consider them as the *intrinsic* Berry phase contribution.³⁶ Our target system, BST, is a topological material, and thus its topological bands such as Dirac Fermion may support Berry curvature in small Fermi energy. Our DFT calculations present significant anomalous Hall conductivity (AHC) via Berry curvature-based Kubo formula. The central results such as no sign change with varying chemical potential and temperature are consistent with the gate-dependent AHE loops. Therefore, both our experimental and theoretical investigation have provided compelling evidence that the AHE in BST/EuIG is most likely attributed to the intrinsic Berry phase contribution.

Gate and Temperature Dependence of the Topological Hall Effect-Like Feature. When the electron flows through the spin texture such as skyrmion, it can acquire a

nonvanishing Berry phase, leading to the “extra” Hall signal on the AHE loop, known as the THE.²⁵ AHE loops of *sample E* in Figure 4b also reveal “extra” Hall signals near the H_{c1} that gained strength with V_{gate} varying from −10 to +3 V. However, a few works found that *alleged* THE responses in TI systems may arise from the two AHE contributions, and the sign of AHE loops does not remain the same with varying gate voltage and temperature.^{41,42} Hence, we added Figure S10 in the Supporting Information to address this issue and to clarify the controversy. We called the “extra” Hall signal as “the THE-like feature” since our evidence for the THE is not rigorous, where we do not probe the spin textures directly.

As discussed in Figure 4b, with decreasing the thickness of BST from 7 to 4 nm, two H_c 's (H_{c1} and H_{c2}) appear in all AHE loops. The top and bottom SSs of BST are both magnetized, so it is expected that the two SSs may result in the two AHE contributions with the same sign. After subtracting the two-AHE component as discussed in Figure S11, Supporting Information, the extracted THE-like resistance ($R_{\text{THE-like}}$) is ~4.5 Ω ($\rho_{\text{THE-like}} \sim 1.8 \mu\Omega \cdot \text{cm}$) as shown in Figure 6a. The gate-dependent $R_{\text{THE-like}}$ at 2 K is displayed in Figure 6b. The THE-like feature is more pronounced in the hole-doped region, and $R_{\text{THE-like}}$ has a maximum value ~4.5 Ω at V_{gate} of −3 V. Note that the magnitudes of our ρ_{AHE} and $\rho_{\text{THE-like}}$ are ~2.0 and ~1.8 $\mu\Omega \cdot \text{cm}$, respectively at 2 K, about 8–11 times larger than those of $\text{Bi}_2\text{Se}_3/\text{BaFe}_{12}\text{O}_{19}$.²⁶

Recently Jiang et al. reported in gated Cr-BST/BST/Cr-BST sandwiched heterostructures the appearance of THE in the QAH insulating regime resulting from the gate-induced DMI during the magnetization reversal process.³³ Their calculations found a large spin susceptibility that emerges from the bulk valence band to enhance the DMI significantly.³³ On the same token, our observation of a gate-induced THE-like feature in the AHE regime at negative V_{gate} may also be attributed to the same reason when the E_F of BST is located in the bulk valence band.

Figure 6c shows the gate-dependent R_{AHE} and $R_{\text{THE-like}}$ in temperatures varying from 2 to 15 K. In all temperatures, $R_{\text{THE-like}}$ has a maximum value for V_{gate} at −3 V, and the hump feature becomes smaller or even disappears as the temperature increases. The extracted $R_{\text{THE-like}}$ values from Figure 6c are shown in Figure 6d at the selected V_{gate} . The $R_{\text{THE-like}}$ in all V_{gate} decreases with increasing temperatures, and when the V_{gate} is at −8 and −10 V, THE-like feature disappears at 15 and 10 K, respectively. Notably, our THE-like feature exists only up to 15 K, but the AHE is still observed even at 400 K. If the “extra” Hall signals were composed of two opposite AHE contributions, it should sustain higher temperatures to be concurrent with AHE. The fact that the temperature dependence of THE-like feature is vastly different from that of AHE suggests that the THE-like feature and AHE originate from two different mechanisms.

The temperature dependence of the THE-like features could be described by reduced DMI strength at a higher temperature. The formation of skyrmions requires $D \geq \frac{4}{\pi} \sqrt{AK}$, where D , A , and K are the DMI constant, exchange constant, and perpendicular anisotropy constant, respectively. As the temperature increases, the decrease in D may be more than the decrease in A and K . Therefore, it is expected that the THE feature disappears quickly with the temperature exceeding a critical temperature.²⁶ This is consistent with our experiment results shown in Figure 6d. Overall, the temperature

dependence of the THE-like features may be far more sensitive than that of AHE as we have discovered in this work.

CONCLUSIONS

We have demonstrated BST/EuIG heterostructures with outstanding materials characteristics, magneto-transport features, and theoretical calculations. Notably, the sign of R_{AHE} remains negative with varying chemical potential, and the enormous magnitude of ρ_{AHE} exceeds the previous record at room temperature by 20 times, sustaining to 400 K. These striking results are well interpreted by our DFT calculations based on an artificially applied Zeeman field plus a contact potential on BST. Therefore, our ability to produce these tailored magnetic TI heterostructures in conjunction with the theoretical guidance for interface tuning has provided a promising way to realize topologically distinct phenomena such as the THE and topological magnetoelectric effect (TME) in axion insulators,⁴³ etc. Note that there remain challenges to achieving the QAHE in TI/MI bilayer structures, and we delineate the possible reasons for this in the Supporting Information. More simulations and experiments of the QAHE in such bilayer or even trilayer structures are left as an open question for future pursuits. The coexistence of AHE and THE may provide a platform to investigate the correlation between chiral edge states and chiral spin textures. It will lead to TI-based dissipation-less and low-power spintronics in the future, realizing these TI materials for practical applications.

EXPERIMENTAL METHODS

Materials Growth. Ferrimagnetic insulator EuIG thin films were grown on GGG substrates in (001) orientation using the off-axis magnetron sputtering technique.²⁴ The EuIG samples were transferred to a standard molecular beam epitaxy (MBE) system with a base pressure of 4×10^{-10} Torr, and annealed at temperatures varying from 450 to 750 °C. After the EuIG films were cooled to room temperature, the BST film growth commenced by evaporation from high purity (99.9999%) Bi, Sb, and Te sources. The crystallinity of the BST thin film surface was monitored by RHEED patterns during the growth, and the Bi:Sb composition ratio was kept at 3:7 to control the E_F close to the exchange gap with a growth rate of 0.36 nm/min.

Characterization. The surface morphologies of the annealed EuIG and BST/EuIG samples were examined by AFM using the noncontact mode. The epitaxial relationship between BST, EuIG, and GGG was studied using synchrotron-radiation XRD at BL17B beamline ($\lambda = 1.5498 \text{ \AA}$) of Taiwan Light Source, Hsinchu, Taiwan. The BST/EuIG interface was characterized by Cs-STEM using a HAADF detector. The experiments were performed on an aberration-corrected (a 0.9 Å probe size) JEOL 2100F, operated at an accelerating voltage of 200 kV. The STEM samples were prepared by using mechanical polishing and focused ion beam. The atomic models in Figure 1f were drawn with the VESTA software. Notice that the excessive oxygen positions in the structural model on the STEM image are not shown for simplicity.

Electrical Measurements. The BST/EuIG samples were patterned into Hall bar devices ($650 \mu\text{m} \times 50 \mu\text{m}$) by photolithography and reactive ion etching. Four-terminal Hall measurements from 10 to 400 K were conducted in a Quantum Design physical property measurement system (PPMS) using a 30 μA direct current source. The top-gate sample fabrication and measurements are described in Figure S6, Supporting Information. In Hall measurements, R_{xx} often mixes with R_{HE} because of the misalignment of contact electrodes. To remove this effect, the “anti-symmetrization method” was carried out for all Hall traces $R_{\text{HE}}(H) = \frac{R_{\text{HE}}^{\text{raw}}(H) - R_{\text{HE}}^{\text{raw}}(-H)}{2}$.

First-Principles Calculations in BST. First-principles electronic property calculations of Bi_2Te_3 (Sb_2Te_3) were performed using the

projector augmented wave (PAW) potentials within the standard DFT framework as implemented in the Vienna *ab initio* Simulation Package (VASP).^{44–46} In the calculations of electronic structures, the SOC was included self-consistently with a Monkhorst–Pack *k*-point grid of size $13 \times 13 \times 5$. To systematically calculate the bulk and surface electronic structures, and AHC in a few QLs of $(\text{Bi},\text{Sb})_2\text{Te}_3$, we constructed a tight-binding Hamiltonian for both Bi_2Te_3 and Sb_2Te_3 by projecting onto the Wannier orbitals,^{47–49} which used the VASP2WANNIER90 interface.⁵⁰ For generating the Wannier functions of a real space tight-binding model of Bi_2Te_3 and Sb_2Te_3 , we used Bi (p-orbitals), Sb (p-orbitals), and Te (p-orbitals) without performing the procedure for maximally localized Wannier functions. The electronic structure of the $(\text{Bi},\text{Sb})_2\text{Te}_3$ with $\text{Bi}:\text{Sb} = 3:7$ was calculated by linear interpolation of tight-binding model matrix elements of Bi_2Te_3 and Sb_2Te_3 . This approach was successfully applied to investigate the evolution of band topology in $\text{BiTlSe}_{1-x}\text{S}_x$ TIs and $\text{Mo}_x\text{W}_{1-x}\text{Te}_2$ Weyl semimetals. In addition, when the chemical potential is away from the exchange gap and crosses the bulk bands, it is not clear whether the intrinsic AHE is still dominant in this system. The AHC calculated in this work is in a range of chemical potential from -0.1 to 0.1 eV, near or located in the exchange gap.

ASSOCIATED CONTENT

Supporting Information

The Supporting Information is available free of charge at <https://pubs.acs.org/doi/10.1021/acsnano.1c08663>.

Material characterizations at various T_a , discussions on suppressed weak antilocalization, origin of AHE signals, top-gate device fabrication, gate-dependent Hall effect data, DFT calculations, “the THE-like data”, and the absence of QAHE at 2 K ([PDF](#))

AUTHOR INFORMATION

Corresponding Authors

Jueinai Kwo – Department of Physics, National Tsing Hua University, Hsinchu 30013, Taiwan; Email: raynien@phys.nthu.edu.tw

Minghwei Hong – Graduate Institute of Applied Physics and Department of Physics, National Taiwan University, Taipei 10617, Taiwan; Email: mhong@phys.ntu.edu.tw

Tay-Rong Chang – Department of Physics, National Cheng Kung University, Tainan 701, Taiwan; Physics Division, National Center for Theoretical Sciences, National Taiwan University, Taipei 10617, Taiwan; Center for Quantum Frontiers of Research and Technology (QFort), Tainan 701, Taiwan; [orcid.org/0000-0003-1222-2527](#); Email: u32trc00@phys.ncku.edu.tw

Authors

Wei-Jihh Zou – Department of Physics, National Tsing Hua University, Hsinchu 30013, Taiwan; [orcid.org/0000-0002-8335-3711](#)

Meng-Xin Guo – Department of Physics, National Tsing Hua University, Hsinchu 30013, Taiwan

Jyun-Fong Wong – Department of Physics, National Tsing Hua University, Hsinchu 30013, Taiwan

Zih-Ping Huang – Graduate Institute of Applied Physics and Department of Physics, National Taiwan University, Taipei 10617, Taiwan

Jui-Min Chia – Department of Physics, National Tsing Hua University, Hsinchu 30013, Taiwan

Wei-Nien Chen – Department of Physics, National Tsing Hua University, Hsinchu 30013, Taiwan

Sheng-Xin Wang – Department of Physics, National Tsing Hua University, Hsinchu 30013, Taiwan

Keng-Yung Lin – Graduate Institute of Applied Physics and Department of Physics, National Taiwan University, Taipei 10617, Taiwan

Lawrence Boyu Young – Graduate Institute of Applied Physics and Department of Physics, National Taiwan University, Taipei 10617, Taiwan; [orcid.org/0000-0003-2569-6094](#)

Yen-Hsun Glen Lin – Graduate Institute of Applied Physics and Department of Physics, National Taiwan University, Taipei 10617, Taiwan

Mohammad Yahyavi – Department of Physics, National Cheng Kung University, Tainan 701, Taiwan

Chien-Ting Wu – Materials Analysis Division, Taiwan Semiconductor Research Institute, National Applied Research Laboratories, Hsinchu 300091, Taiwan

Horng-Tay Jeng – Department of Physics, National Tsing Hua University, Hsinchu 30013, Taiwan; Institute of Physics, Academia Sinica, Taipei 11529, Taiwan; Physics Division, National Center for Theoretical Sciences, National Taiwan University, Taipei 10617, Taiwan; [orcid.org/0000-0002-2881-3826](#)

Shang-Fan Lee – Institute of Physics, Academia Sinica, Taipei 11529, Taiwan; [orcid.org/0000-0001-5899-7200](#)

Complete contact information is available at:

<https://pubs.acs.org/10.1021/acsnano.1c08663>

Author Contributions

○W.-J.Z., M.-X.G., J.-F.W., Z.-P.H., and J.-M.C. contributed equally to this work. W.-J.Z., J.-F.W., and J.-M.C. collected the transport data and analyzed the data. M.-X.G., Z.-P.H., S.-X.W., L.-B.Y., and Y.-H.G.L. fabricated the samples. W.-N.C. performed the XRD measurements. K.-Y.L. performed the XPS measurements. M.Y. did the theoretical calculations. C.-T.W. performed the STEM measurements. T.-R.C. and S.-F.L. provided scientific supports. J.K. and M.H. supervised the project. W.-J.Z., J.-F.W., and J.K. wrote the manuscript with the comments of all the authors.

Notes

A previous version of this manuscript has been submitted to a preprint server.⁵¹

The authors declare no competing financial interest.

ACKNOWLEDGMENTS

The authors would like to thank C.-Y. Mou, H.-H. Lin, C.-F. Pai, C.-H. Hsu, Y.-C. Liu, C.-C. Chen, K.-H. M. Chen, J.-K. Cheng, and S.-W. Huang for helpful discussions. Technical support from NGPL/IOP/Academia Sinica, NSRRC, TSR, and the NTU Consortium of Electron Microscopy Key Technology, Taiwan, are acknowledged. This work was financially supported by the Ministry of Science and Technology (MOST), Taiwan, with project numbers 105-2112-M-007-014-MY3, 109-2112-M-002-028, and 109-2622-8-002-003, Center of Quantum Technology, NTHU, with project number XXX109B0022I4, and the Thematic Project AS-TP-107-M04, Academia Sinica, Taiwan. T.-R.C. was supported by the Young Scholar Fellowship Program from the MOST in Taiwan, under a MOST grant for the Columbus Program, no. MOST110-2636-M-006-016, NCKU, Taiwan, and National Center for Theoretical Sciences, Taiwan. Work at NCKU was supported by the MOST, Taiwan, under grant no. MOST107-2627-E-006-001 and Higher Education Sprout

Project, Ministry of Education to the Headquarters of University Advancement at NCKU.

REFERENCES

- (1) Qi, X.-L.; Hughes, T. L.; Zhang, S.-C. Topological Field Theory of Time-Reversal Invariant Insulators. *Phys. Rev. B* **2008**, *78*, 195424.
- (2) Hasan, M. Z.; Kane, C. L. Colloquium: Topological Insulators. *Rev. Mod. Phys.* **2010**, *82*, 3045.
- (3) Yu, R.; Zhang, W.; Zhang, H.-J.; Zhang, S.-C.; Dai, X.; Fang, Z. Quantized Anomalous Hall Effect in Magnetic Topological Insulators. *Science* **2010**, *329*, 61–64.
- (4) Chang, C.-Z.; Zhang, J.; Feng, X.; Shen, J.; Zhang, Z.; Guo, M.; Li, K.; Ou, Y.; Wei, P.; Wang, L.-L.; Ji, Z.-Q.; Feng, Y.; Ji, S.; Chen, X.; Jia, J.; Dai, X.; Fang, Z.; Zhang, S.-C.; He, K.; Wang, Y.; et al. Experimental Observation of the Quantum Anomalous Hall Effect in a Magnetic Topological Insulator. *Science* **2013**, *340*, 167–170.
- (5) Tokura, Y.; Yasuda, K.; Tsukazaki, A. Magnetic Topological Insulators. *Nat. Rev. Phys.* **2019**, *1*, 126–143.
- (6) Kou, X.; Guo, S.-T.; Fan, Y.; Pan, L.; Lang, M.; Jiang, Y.; Shao, Q.; Nie, T.; Murata, K.; Tang, J.; Wang, Y.; He, L.; Lee, T.-K.; Lee, W.-L.; Wang, K. L. Scale-Invariant Quantum Anomalous Hall Effect in Magnetic Topological Insulators beyond the Two-Dimensional Limit. *Phys. Rev. Lett.* **2014**, *113*, 137201.
- (7) Checkelsky, J. G.; Yoshimi, R.; Tsukazaki, A.; Takahashi, K. S.; Kozuka, Y.; Falson, J.; Kawasaki, M.; Tokura, Y. Trajectory of the Anomalous Hall Effect towards the Quantized State in a Ferromagnetic Topological Insulator. *Nat. Phys.* **2014**, *10*, 731–736.
- (8) Chang, C.-Z.; Zhao, W.; Kim, D. Y.; Zhang, H.; Assaf, B. A.; Heiman, D.; Zhang, S.-C.; Liu, C.; Chan, M. H. W.; Moodera, J. S. High-Precision Realization of Robust Quantum Anomalous Hall State in a Hard Ferromagnetic Topological Insulator. *Nat. Mater.* **2015**, *14*, 473–477.
- (9) Kandala, A.; Richardella, A.; Kempinger, S.; Liu, C.-X.; Samarth, N. Giant Anisotropic Magnetoresistance in a Quantum Anomalous Hall Insulator. *Nat. Commun.* **2015**, *6*, 7434.
- (10) Mogi, M.; Yoshimi, R.; Tsukazaki, A.; Yasuda, K.; Kozuka, Y.; Takahashi, K. S.; Kawasaki, M.; Tokura, Y. Magnetic Modulation Doping in Topological Insulators toward Higher-Temperature Quantum Anomalous Hall Effect. *Appl. Phys. Lett.* **2015**, *107*, 182401.
- (11) Chang, C.-Z.; Tang, P.; Wang, Y.-L.; Feng, X.; Li, K.; Zhang, Z.; Wang, Y.; Wang, L.-L.; Chen, X.; Liu, C.; Duan, W.; He, K.; Ma, X.-C.; Xue, Q.-K. Chemical-Potential-Dependent Gap Opening at the Dirac Surface States of Bi_2Se_3 Induced by Aggregated Substitutional Cr Atoms. *Phys. Rev. Lett.* **2014**, *112*, 056801.
- (12) Wei, P.; Katmis, F.; Assaf, B. A.; Steinberg, H.; Jarillo-Herrero, P.; Heiman, D.; Moodera, J. S. Exchange-Coupling-Induced Symmetry Breaking in Topological Insulators. *Phys. Rev. Lett.* **2013**, *110*, 186807.
- (13) Katmis, F.; Lauter, V.; Nogueira, F. S.; Assaf, B. A.; Jamer, M. E.; Wei, P.; Satpati, B.; Freeland, J. W.; Eremin, I.; Heiman, D.; Jarillo-Herrero, P.; Moodera, J. S. A High-Temperature Ferromagnetic Topological Insulating Phase by Proximity Coupling. *Nature* **2016**, *533*, 513–516.
- (14) Lang, M.; Montazeri, M.; Onbasli, M. C.; Kou, X.; Fan, Y.; Upadhyaya, P.; Yao, K.; Liu, F.; Jiang, Y.; Jiang, W.; Wong, K. L.; Yu, G.; Tang, J.; Nie, T.; He, L.; Schwartz, R. N.; Wang, Y.; Ross, C. A.; Wang, K. L. Proximity Induced High-Temperature Magnetic Order in Topological Insulator - Ferrimagnetic Insulator Heterostructure. *Nano Lett.* **2014**, *14*, 3459–3465.
- (15) Bhattacharyya, S.; Akhgar, G.; Gebert, M.; Karel, J.; Edmonds, M. T.; Fuhrer, M. S. Recent Progress in Proximity Coupling of Magnetism to Topological Insulators. *Adv. Mater.* **2021**, *33*, e2007795.
- (16) Tang, C.; Chang, C.-Z.; Zhao, G.; Liu, Y.; Jiang, Z.; Liu, C.-X.; McCartney, M. R.; Smith, D. J.; Chen, T.; Moodera, J. S.; Shi, J. Above 400-K Robust Perpendicular Ferromagnetic Phase in a Topological Insulator. *Sci. Adv.* **2017**, *3*, e1700307.
- (17) Chen, C. C.; Chen, K. H. M.; Fanchiang, Y. T.; Tseng, C. C.; Yang, S. R.; Wu, C. N.; Guo, M. X.; Cheng, C. K.; Huang, S. W.; Lin, K. Y.; Wu, C. T.; Hong, M.; Kwo, J. Topological Insulator Bi_2Se_3 Films on Rare Earth Iron Garnets and Their High-Quality Interfaces. *Appl. Phys. Lett.* **2019**, *114*, 031601.
- (18) Tang, C.; Sellappan, P.; Liu, Y.; Xu, Y.; Garay, J. E.; Shi, J. Anomalous Hall Hysteresis in $\text{Tm}_3\text{Fe}_5\text{O}_{12}/\text{Pt}$ with Strain-Induced Perpendicular Magnetic Anisotropy. *Phys. Rev. B* **2016**, *94*, 140403.
- (19) Avci, C. O.; Quindeau, A.; Pai, C.-F.; Mann, M.; Caretta, L.; Tang, A. S.; Onbasli, M. C.; Ross, C. A.; Beach, G. S. D. Current-Induced Switching in a Magnetic Insulator. *Nat. Mater.* **2017**, *16*, 309–314.
- (20) Wu, C. N.; Tseng, C. C.; Lin, K. Y.; Cheng, C. K.; Yeh, S. L.; Fanchiang, Y. T.; Hong, M.; Kwo, J. High-Quality Single-Crystal Thulium Iron Garnet Films with Perpendicular Magnetic Anisotropy by Off-Axis Sputtering. *AIP Advances* **2018**, *8*, 055904.
- (21) Wu, C. N.; Tseng, C. C.; Fanchiang, Y. T.; Cheng, C. K.; Lin, K. Y.; Yeh, S. L.; Yang, S. R.; Wu, C. T.; Liu, T.; Wu, M.; Hong, M.; Kwo, J. High-Quality Thulium Iron Garnet Films with Tunable Perpendicular Magnetic Anisotropy by Off-Axis Sputtering – Correlation between Magnetic Properties and Film Strain. *Sci. Rep.* **2018**, *8*, 11087.
- (22) Rosenberg, E. R.; Beran, L.; Avci, C. O.; Zeledon, C.; Song, B.; Gonzalez-Fuentes, C.; Mendil, J.; Gambardella, P.; Veis, M.; Garcia, C.; Beach, G. S. D.; Ross, C. A. Magnetism and Spin Transport in Rare-Earth-Rich Epitaxial Terbium and Europium Iron Garnet Films. *Phys. Rev. Mater.* **2018**, *2*, 094405.
- (23) Ortiz, V. H.; Aldosary, M.; Li, J.; Xu, Y.; Lohmann, M. I.; Sellappan, P.; Kodera, Y.; Garay, J. E.; Shi, J. Systematic Control of Strain-Induced Perpendicular Magnetic Anisotropy in Epitaxial Europium and Terbium Iron Garnet Thin Films. *APL Mater.* **2018**, *6*, 121113.
- (24) Guo, M. X.; Cheng, C. K.; Liu, Y. C.; Wu, C. N.; Chen, W. N.; Chen, T. Y.; Wu, C. T.; Hsu, C. H.; Zhou, S. Q.; Chang, C. F.; Tjeng, L. H.; Lee, S. F.; Pai, C. F.; Hong, M.; Kwo, J. Single-crystal epitaxial europium iron garnet films with strain-induced perpendicular magnetic anisotropy: structural, strain, magnetic, and spin transport properties. *arXiv.org*, **2022**; Ver. 1, 2201.03843, <https://arxiv.org/abs/2201.03843>.
- (25) Nagaosa, N.; Tokura, Y. Topological Properties and Dynamics of Magnetic Skyrmions. *Nat. Nanotechnol.* **2013**, *8*, 899–911.
- (26) Li, P.; Ding, J.; Zhang, S. S.-L.; Kally, J.; Pillsbury, T.; Heinonen, O. G.; Rimal, G.; Bi, C.; DeMann, A.; Field, S. B.; Wang, W.; Tang, J.; Jiang, J. S.; Hoffmann, A.; Samarth, N.; Wu, M. Topological Hall Effect in a Topological Insulator Interfaced with a Magnetic Insulator. *Nano Lett.* **2021**, *21*, 84–90.
- (27) Fert, A.; Cros, V.; Sampaio, J. Skyrmions on the Track. *Nat. Nanotechnol.* **2013**, *8*, 152–156.
- (28) Iida, S. Magnetostriction Constants of Rare Earth Iron Garnets. *J. Phys. Soc. Jpn.* **1967**, *22*, 1201–1209.
- (29) Mokarian Zanjani, S.; Onbasli, M. C. Predicting New Iron Garnet Thin Films with Perpendicular Magnetic Anisotropy. *J. Magn. Magn.* **2020**, *499*, 166108.
- (30) Watanabe, R.; Yoshimi, R.; Kawamura, M.; Mogi, M.; Tsukazaki, A.; Yu, X. Z.; Nakajima, K.; Takahashi, K. S.; Kawasaki, M.; Tokura, Y. Quantum Anomalous Hall Effect Driven by Magnetic Proximity Coupling in All-Telluride Based Heterostructure. *Appl. Phys. Lett.* **2019**, *115*, 102403.
- (31) Chang, C.-Z.; Zhang, J.; Liu, M.; Zhang, Z.; Feng, X.; Li, K.; Wang, L.-L.; Chen, X.; Dai, X.; Fang, Z.; Qi, X.-L.; Zhang, S.-C.; Wang, Y.; He, K.; Ma, X.-C.; Xue, Q.-K. Thin Films of Magnetically Doped Topological Insulator with Carrier-Independent Long-Range Ferromagnetic Order. *Adv. Mater.* **2013**, *25*, 1065.
- (32) Liu, C.; Zang, Y.; Ruan, W.; Gong, Y.; He, K.; Ma, X.; Xue, Q.-K.; Wang, Y. Dimensional Crossover-Induced Topological Hall Effect in a Magnetic Topological Insulator. *Phys. Rev. Lett.* **2017**, *119*, 176809.
- (33) Jiang, J.; Xiao, D.; Wang, F.; Shin, J.-H.; Andreoli, D.; Zhang, J.; Xiao, R.; Zhao, Y.-F.; Kayyalha, M.; Zhang, L.; Wang, K.; Zang, J.; Liu, C.; Samarth, N.; Chan, M. H. W.; Chang, C.-Z. Concurrence of Quantum Anomalous Hall and Topological Hall Effects in Magnetic

Topological Insulator Sandwich Heterostructures. *Nat. Mater.* **2020**, *19*, 732.

(34) Hao, Q.; Xiao, G. Giant Spin Hall Effect and Magnetotransport in a Ta/CoFeB/MgO Layered Structure: A Temperature Dependence Study. *Phys. Rev. B* **2015**, *91*, 224413.

(35) Shao, Q.; Grutter, A.; Liu, Y.; Yu, G.; Yang, C.-Y.; Gilbert, D. A.; Arenholz, E.; Shafer, P.; Che, X.; Tang, C.; Aldosary, M.; Navabi, A.; He, Q. L.; Kirby, B. J.; Shi, J.; Wang, K. L. Exploring Interfacial Exchange Coupling and Sublattice Effect in Heavy Metal/Ferrimagnetic Insulator Heterostructures Using Hall Measurements, X-Ray Magnetic Circular Dichroism, and Neutron Reflectometry. *Phys. Rev. B* **2019**, *99*, 104401.

(36) Nagaosa, N.; Sinova, J.; Onoda, S.; MacDonald, A. H.; Ong, N. P. Anomalous Hall Effect. *Rev. Mod. Phys.* **2010**, *82*, 1539.

(37) Jiang, Z.; Chang, C.-Z.; Tang, C.; Wei, P.; Moodera, J. S.; Shi, J. Independent Tuning of Electronic Properties and Induced Ferromagnetism in Topological Insulators with Heterostructure Approach. *Nano Lett.* **2015**, *15*, 5835–5840.

(38) Guo, G. Y.; Yao, Y.; Niu, Q. *ab Initio* Calculation of the Intrinsic Spin Hall Effect in Semiconductors. *Phys. Rev. Lett.* **2005**, *94*, 226601.

(39) Wang, Q.-Z.; Liu, X.; Zhang, H.-J.; Samarth, N.; Zhang, S.-C.; Liu, C.-X. Quantum Anomalous Hall Effect in Magnetically Doped InAs/GaSb Quantum Wells. *Phys. Rev. Lett.* **2014**, *113*, 147201.

(40) Rashba, E. I. Side jump contribution to spin-orbit mediated hall effects and berry curvature. *Semiconductors* **2008**, *42*, 905.

(41) Fijalkowski, K. M.; Hartl, M.; Winnerlein, M.; Mandal, P.; Schreyeck, S.; Brunner, K.; Gould, C.; Molenkamp, L. W. Coexistence of Surface and Bulk Ferromagnetism Mimics Skyrmion Hall Effect in a Topological Insulator. *Phys. Rev. X* **2020**, *10*, 011012.

(42) Wang, F.; Wang, X.; Zhao, Y.-F.; Xiao, D.; Zhou, L.-J.; Liu, W.; Zhang, Z.; Zhao, W.; Chan, M. H. W.; Samarth, N.; Liu, C.; Zhang, H.; Chang, C.-Z. Interface-induced sign reversal of the anomalous Hall effect in magnetic topological insulator heterostructures. *Nat. Commun.* **2021**, *12*, 79.

(43) Gao, A.; Liu, Y.-F.; Hu, C.; Qiu, J.-X.; Tzschaschel, C.; Ghosh, B.; Ho, S.-C.; Bérubé, D.; Chen, R.; Sun, H.; Zhang, Z.; Zhang, X.-Y.; Wang, Y.-X.; Wang, N.; Huang, Z.; Felser, C.; Agarwal, A.; Ding, T.; Tien, H.-J.; Akey, A.; et al. Layer Hall Effect in a 2D Topological Axion Antiferromagnet. *Nature* **2021**, *595*, 521–525.

(44) Kresse, G.; Furthmüller, J. Efficient Iterative Schemes for *ab Initio* Total-Energy Calculations Using a Plane-Wave Basis Set. *Phys. Rev. B* **1996**, *54*, 11169.

(45) Kresse, G.; Joubert, D. From Ultrasoft Pseudopotentials to the Projector Augmented-Wave Method. *Phys. Rev. B* **1999**, *59*, 1758.

(46) Blöchl, P. E. Projector Augmented-Wave Method. *Phys. Rev. B* **1994**, *50*, 17953.

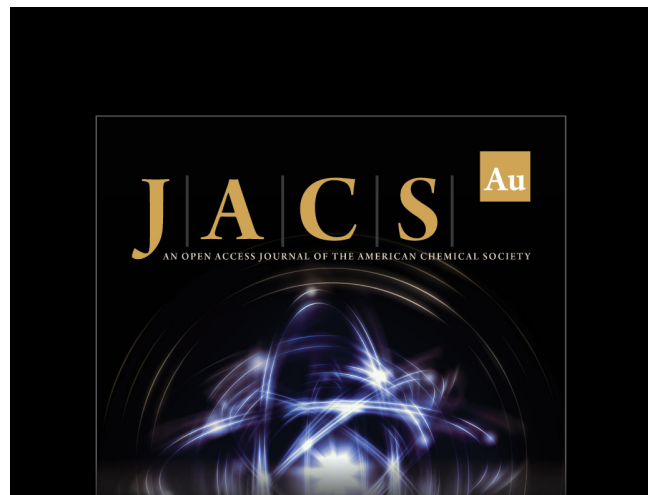
(47) Marzari, N.; Vanderbilt, D. Maximally Localized Generalized Wannier Functions for Composite Energy Bands. *Phys. Rev. B* **1997**, *56*, 12847.

(48) Souza, I.; Marzari, N.; Vanderbilt, D. Maximally Localized Wannier Functions for Entangled Energy Bands. *Phys. Rev. B* **2001**, *65*, 035109.

(49) Mostofi, A. A.; Yates, J. R.; Lee, Y.-S.; Souza, I.; Vanderbilt, D.; Marzari, N. Wannier90: A Tool for Obtaining Maximally-Localised Wannier Functions. *Comput. Phys. Commun.* **2008**, *178*, 685–699.

(50) Franchini, C.; Kovacik, R.; Marsman, M.; Sathyaranayana Murthy, S.; He, J.; Ederer, C.; Kresse, G. Maximally Localized Wannier Functions in LaMnO₃ within PBE + U, Hybrid Functionals and Partially Self-Consistent GW: an Efficient Route to Construct *ab Initio* Tight-Binding Parameters for e_g Perovskites. *J. Phys.: Condens. Matter* **2012**, *24*, 235602.

(51) Zou, W.-J.; Guo, M.-X.; Wong, J.-F.; Huang, Z.-P.; Chia, J.-M.; Chen, W.-N.; Wang, S.-X.; Lin, K.-Y.; Young, L. B.; Lin, Y.-H. G.; Yahyavi, M.; Wu, C.-T.; Jeng, H.-T.; Lee, S.-F.; Chang, T.-R.; Hong, M.; Kwo, J. Enormous Berry-Curvature-Driven Anomalous Hall Effect in Topological Insulator (Bi,Sb)₂Te₃ on Ferrimagnetic Europium Iron Garnet beyond 400 K. *arXiv.org*, **2021**; Ver. 4, 2103.16487, <https://arxiv.org/abs/2103.16487>.



Editor-in-Chief
Prof. Christopher W. Jones
Georgia Institute of Technology, USA

Open for Submissions